Article

Colloidal Self-Assembly of Highly-Ordered Silica Inverse Opals for Deep Ultraviolet Diffraction

Ivan G. Pallares,*,[†] Dipak Rout,[†] Thomas J. Deering, Kyle T. Hufziger, Sergei V. Bykov, and Sanford A. Asher*

Read Online

ACCESS | Metrics & More | Article Recommendations | Supporting Information

ABSTRACT: The fabrication of highly ordered ∼2 μm thick silica inverse opal (IO) photonic crystal (PhC) films is reported. These IO films diffract deep ultraviolet light (UV, <250 nm) and are prepared using the inward-growing self-assembly of ∼143 nm diameter monodisperse polystyrene nanoparticles (PSNPs) suspended within a hydrolyzed silicate sol−gel precursor solution. Removal of the PSNPs results in solid, robust IOs that attenuate >70% of light meeting the Bragg condition at normal incidence. Structural and optical character- ization of these silica IO films indicate that noncoherent scattering losses are low at deep UV wavelengths, even though substantial crack- type defects occur. The IO films exhibit a diffraction fwhm of ∼12 nm with diffraction efficiencies of >30% for 213 nm laser light and possess nanoscale porosities of ∼20 nm. Relative to reported silica IOs that diffract deep UV light, these new PhC materials show at least 28% narrower spectral bandwidths and 5-fold increased diffraction efficiencies. We postulate that increased ordering of the silica network is the principal factor that improves the optical performance. Furthermore, the relatively flat, homogeneous IO film surfaces produce narrow, symmetric diffraction beams suitable for optical imaging applications. Strategies to further improve the diffraction efficiencies of these silica IO materials and the implications for novel technological applications are discussed.

KEYWORDS: photonic crystals, inverse opals, colloidal self-assembly, ultraviolet diffraction, nanoporous, silica sol−gel

INTRODUCTION

The development of deep UV ($\lambda \sim 190-250$ nm) spectroscopic methods is currently hindered by a lack of high-performance optical devices operating in this spectral region.[1−3] For example, developing compact deep UV Raman spectrometers requires efficient optical filters to reject the intense Rayleigh scattered light that can obscure the >10^7-fold weaker Raman bands.[4] There is also a lack of wavelength-selective devices (WSDs) that can efficiently manipulate deep UV light, particularly to select narrow Raman bands for imaging applications.[5−7] In general, the fabrication of optical devices operating in the deep UV is limited by the absorption of UV light by most materials. New technologies for the development of deep UV optical elements have recently been pioneered by developing photonic crystals (PhCs) that diffract in the UV region.[7]

PhCs selectively restrict particular wavelengths of light from propagating due to the presence of photonic band gaps.[8,9] These PhC properties have been exploited to increase the efficiency of solar energy harvesting,[10,11] to demonstrate low-threshold lasing,[12−14] and for chemical and biochemical sensing applications.[15,16] The presence of a photonic stop band in PhCs results in the diffraction of particular incident

light wavelengths, making these materials useful for spectro-scopic applications.[17,18]

We previously demonstrated the use of PhCs with stop bands in the deep UV for Rayleigh rejection filters for 229 nm light.[6,7] Furthermore, we recently demonstrated the use of PhCs as WSDs for the development of the first deep UV wide-field Raman imaging spectrometer for standoff detection of trace explosives.[3] These deep UV optical devices consisted of crystalline colloidal arrays (CCAs) of highly charged, monodisperse silica nanoparticles suspended in water.
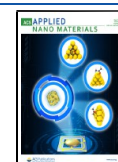
Silica is an ideal material for such devices because it does not significantly absorb deep UV light.[19] However, implementation of CCAs for deep UV spectroscopic instrumentation is hindered by their limited robustness, as extended UV irradiation can lead to degradation of the CCAs. In practice, the optical properties of CCAs are also sensitive to mechanical
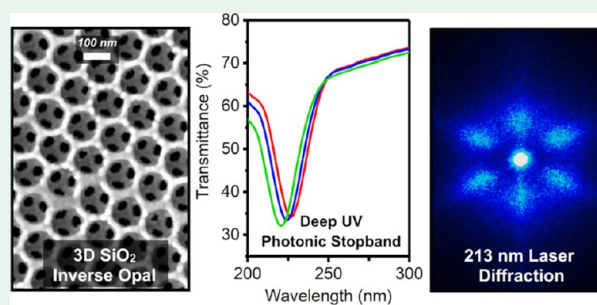
vibrations, temperature inhomogeneities, and solvent motion, all of which can transiently alter the interparticle spacings.

Our group recently reported a modified vertical self-assembly method to fabricate solid inverse opals (IOs) composed of air spheres in a close-packed face-centered-cubic (fcc) structure within a silica network.[20] These PhCs were shown to possess a photonic stop band in the deep UV region with a ~7% diffraction efficiency for 229 nm light. While this fabrication method yielded PhCs that were more stable to UV radiation, their imperfect optical properties limited their use as optical devices. Specifically, these PhCs possessed surface striations arising from the stick−slip mechanism inherent to vertical self-assembly. The variations in the surface morphology give rise to interfering diffraction patterns that obscure the expected diffraction spots.[20] These PhCs also attenuated light at UV wavelengths outside the first-order stop band. For example, we observed ~90% light attenuation at 200 nm. This incoherent scattering strongly overlaps with light diffraction from the stop band.

Inward-growing self-assemblies of close-packed PSNP arrays have also been reported.[21] However, the feasibility of these methods for generating SiO_2 IOs that diffract in the deep-UV has not been shown. The determination of the diffraction efficiencies and noncoherent scattering loses of the resulting SiO_2 IOs is also lacking in the literature. These metrics are critical for evaluating the long-range crystalline ordering of these materials. In this work, we describe an alternative method to fabricate silica IOs that diffract deep UV light using an adaptation of inward-growing self-assembly (Figure 1).[21,22] Similarly to our previous report, we use polystyrene nano-particles (PSNPs) to template a close-packed fcc structure in the presence of a tetraethylorthosilicate (TEOS) silica sol−gel precursor. Condensation of the silicates into a solid network, followed by the removal of the PSNPs yields a silica IO. The resulting silica IOs efficiently diffract deep UV light, and are structurally stable. Using detailed spectroscopic character-ization, we report that IOs fabricated by this method show diffraction efficiencies >30% in the deep UV, representing the highest value reported to date. We also report increased transmission of deep UV light outside of the stop band regions, a factor critical for optical applications. Compared to vertically self-assembled IOs, the shape of the diffracted beams is minimally distorted. The diffraction patterns from our IOs are more similar to the diffraction from highly ordered CCAs.[23] Furthermore, our results provide guidance with regards to the coassembly of a sacrificial colloidal crystal template within a silica matrix using sol−gel chemistry.

MATERIALS AND METHODS

Fused Silica Substrate Preparation. Fused silica substrates (FSS, GE-124, Technical Glass Product, $25 \times 25 \times 1$ mm³) were cleaned by immersion for 3 h. in a Piranha solution prepared by mixing sulfuric acid (H_2SO_4, 98%, Fisher) and hydrogen peroxide (H_2O_2, 30%, Fisher) in a 3:1 volume ratio. *Caution: This reaction is highly exothermic. Piranha solution is very corrosive and is a strong oxidizer. Take necessary precautions.* Following Piranha treatment, the substrates were rinsed and then submerged in water for 1 h. to wash away and dilute any remaining acid. Prior to use, the substrates were dried in a nitrogen stream.
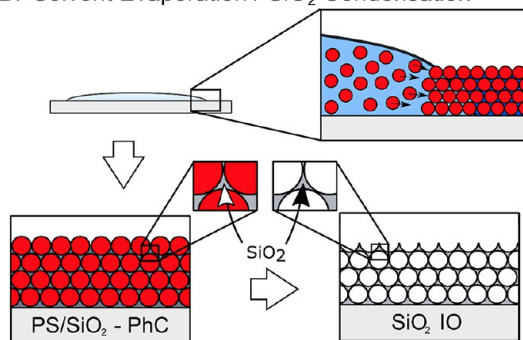
PhC Precursor Solution Preparation. PhC precursor solutions containing ~2.3% v/v PSNPs and 6.0−6.5% v/v silica precursor solutions were prepared in nanopure water (Barnstead Infinity, 18 MΩ•cm). The highly charged PSNPs were synthesized using a modified Reese et al. emulsion polymerization procedure described in

PhC Self-Assembly

A. Deposition of PhC precursor solution.
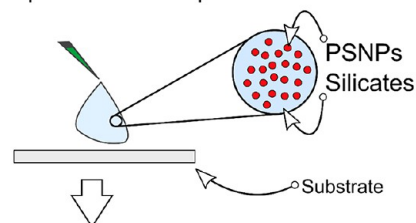
B. Solvent Evaporation / SiO₂ Condensation

C. Removal of PSNPs.

Figure 1. Schematic of the inward-growing self-assembly of a photonic crystal. (A) PhC precursor solution containing polystyrene nanoparticles (PSNPs) and hydrolyzed silicates is deposited onto a clean, hydrophilic substrate. (B) Liquid is evaporated under controlled humidity and temperature conditions. (C) PSNPs are removed to yield a SiO_2 inverse opal photonic crystal.

detail by Hufziger et al.[1,24] The full synthesis details are discussed in the Supporting Information. The silica precursor solution was made by mixing tetraethylorthosilicate (TEOS, Aldrich), hydrochloric acid (HCl, Fisher, diluted to 0.1 M with nanopure water), and ethanol (Decon Laboratories, 200 proof) in a volume ratio of 2:2:3. (Note that the hydrolyzed TEOS solution is ~28% TEOS by volume.) This solution was mixed at 500 rpm with a LP Vortex Mixer (Thermo Fisher) at room temperature (~20 °C) for 3 h. before use.

PhC Fabrication. The cleaned, hydrophilic substrates were placed on a rectangular raised platform inside an environmentally controlled chamber (ECC, Darwin Chambers) equipped with a Vibration Isolation Platform (BT-2024, Newport) as described in Figure S1. Onto each substrate, 200 μL (unless otherwise noted) of a PhC precursor solution was deposited using a pipette. The solutions were observed to spread evenly to cover the substrate, yielding a thin liquid film. The chamber was set to maintain a temperature of 20 °C and a 75% relative humidity environment overnight while the liquid evaporated from the substrates. The airflow inside the ECC was ~180 feet-per-minute (fpm), measured with a Kestrel 3000 weather meter placed on top the sample fabrication platform. To obstruct direct air flow onto the drying substrates, we shielded them under a plastic cover (Rubbermaid, $22 \times 20 \times 12$ cm³). Under the plastic cover, the RH% increased to ~15% above the value in the chamber due to the limited airflow (measured with a Fisher Traceable Hygrometer). The humidity under the air shield equilibrates with that of the chamber once all the visible liquid evaporates. Complete evaporation of the liquid yielded a solid thin film PhC consisting of PSNPs arranged in a close-packed structure with silica embedded in the interstices (PS/SiO_2 PhCs).

The resulting PS/SiO_2 PhCs were maintained at 70 °C for 2 days in a drying oven to remove residual moisture, and to further condense the silica network surrounding the PSNPs. Following this treatment, the PSNPs were removed from the PhCs via immersion in pure tetrahydrofuran (THF, Fisher) for at least 3 h. Following the

treatment with THF, the samples were dried at 20 °C and ~50% RH, before being subsequently submerged in piranha solution overnight to remove the remaining polystyrene. The samples were then placed in a beaker with >200 mL water for 30 min to wash away any piranha solution. Following removal from water, the samples were dried overnight at 20 °C and ~50% RH.

Structural Characterization. PSNPs diameters were measured using transmission electron microscopy (TEM, FEI Morgagni 268). Several microliters of PSNPs were diluted with nanopure water and pipetted onto a Formvar-coated grid (Ted Pella, 01814-F) for imaging. From the images, more than 100 spheres were measured using ImageJ (NIH),[25] yielding an average PSNP diameter of 143 ± 4 nm. We measured the ζ potential to be −41 mV at pH 5 using a Brookhaven ZetaPALS (Smoluchowski approximation).

The surface morphology of the PhCs was characterized by an optical microscope (Olympus) and optical profilometer (Bruker GT). The nanoscale porosity and periodic ordering of the PhCs was imaged using a field emission scanning electron microscope (FESEM, ZEISS Sigma 500) with an ET-SE detector and an accelerating voltage of 3 kV. Samples used for SEM imaging were coated with gold for 75 s (30 mA current) using a sputter coater (PELCO SC-7) to yield a ~15−20 nm thick Au film.

The periodicity of the PhCs was estimated from SEM images by measuring at least 50 center-to-center distances over the area of interest using ImageJ and averaging the results. Side-profile SEM images of PhC were collected to visualize the ordering of the fcc (111) planes and to determine the film thickness and the number of layers.

Optical Characterization. The PhC stop band properties were characterized using a UV−vis-NIR spectrophotometer (Agilent Cary 5000). These measurements were performed in a single beam mode with a 2 nm spectral resolution, a 100 ms. averaging time, and a 600 nm/min scan rate. Samples were mounted on a microscope slide holder (Thorlabs XYFM1) equipped with translational stages to allow sample motion in the plane perpendicular to the incident light beam. This microscope slide holder was attached to a rotational stage (Newport 481-A) to vary the angle of incidence of the light beam relative to the sample normal and to monitor the diffraction as a function of angle.

To estimate the reflectance of the PhC as a function of wavelength, we used a polychromatic Laser Driven Light Source (LDLS, Energetiq, EQ-99X). This device gives rise to a quasi-point source of polychromatic diverging light. We collimated this polychromatic light by using an off-axis parabolic mirror (MPD249-F01, Thorlabs), and directed the light to our fabricated PhC sample mounted on a 2 in. mirror mount (Newport GM-2) attached to a rotational stage (Newport 481-A). The resulting diffracted, scattered and reflected light from the sample was collected by a UV enhanced reflective mirror (RC12SMA-F01, Thorlabs), and directed to an optical fiber coupled UV−vis−NIR spectrograph (QEPro, Ocean Optics). Spectra were collected using <1 ms. integration times and smoothed using the spectrograph boxcar average with a value of 10 pixels.

Angle dependent diffraction measurements were performed by mounting the IO on a rotational stage (Newport 481-A) and measuring the angular dependence of the diffraction power from a 213 nm laser source (UVVisIR, Q-switched diode-pumped solid state Nd:YVO$_4$ laser).[26] The incident angle was rotated by 2° increments about the IO substrate normal, and the corresponding diffracted powers were measured by using a power meter (Thorlabs S120VC head attached to a PM200 console). The measured diffracted power for each incident angle was ratioed to the incident laser power to obtain the diffraction efficiency of our IO PhC. From these power measurements, the angular full-width at half-maximum (fwhm) was used to estimate the diffraction bandwidth. The diffraction pattern from our IO was photographed by directing the diffracted beam onto a fluorescent screen.

RESULTS AND DISCUSSION

We report the fabrication of solid, 3D SiO$_2$ IO PhC films using inward-growing self-assembly of PSNPs in the presence of hydrolyzed TEOS silicate sol−gel precursors. This approach is partially based on previously established methods for generating PhC films from monodisperse colloidal nanoparticle solutions,[21,22] and the coassembly of these structures within a polymer matrix.[20,27,28] Briefly, this method involves the deposition of a PhC precursor solution onto a hydrophilic substrate (Figure 1A). The PhC precursor solution consists of monodisperse PSNPs (143 ± 4 nm in diameter) suspended in an aqueous solution containing hydrolyzed TEOS and HCl. Evaporation of the dispersant liquid under controlled temperature and humidity conditions leads to the formation of close-packed arrays of PSNPs surrounded by a matrix of solidified SiO$_2$ formed by sol−gel condensation (Figure 1B).[21]

Upon removal of the sacrificial PSNPs, a nanoporous SiO$_2$ IO film is obtained with a lattice constant similar to the diameter of the templating PSNPs (Figure 1C). This IO diffracts, but does not significantly absorb, deep UV light.

Notably, this inward-growing self-assembly yields PhC films, which Bragg diffract in the deep UV and show minimal incoherent scattering. Due to the large volume fraction of air in these materials, the average index of refraction of the IOs is much lower than for typical PhCs. This allows for diffraction deeper in the UV relative to PhCs composed of similarly sized solid nanospheres.[29]

In the case of evaporative self-assembly on vertical substrates, the presence of surface striations arranged parallel to the drying front leads to structures with significant incoherent scattering.[20] These striations result in strong scattering of the incident light, producing a large rising background in the extinction spectrum, and a highly distorted diffracted beam.[20,27,30] By minimizing these effects in our SiO$_2$ IO PhCs, the diffraction efficiency in the deep UV is increased relative to that of previous PhC fabrication approaches.[20]

Mechanism of Inward-Growing Self-Assembly. The mechanism of inward-growing self-assembly involves a process by which the evaporation of liquid leads to the spatial redistribution of the dispersed components (i.e., PSNPs and hydrolyzed silicate sol−gel precursors). Various aspects of this overall process are fairly well understood.[31] Notably, because of the hydrophilic substrate surface, the dispersion droplet fully wets the substrate and becomes initially pinned to substrate edges. In this regime, the flow and subsequent deposition of the dispersed species largely follows the so-called "coffee-ring effect".[32] Enhanced evaporation at the perimeter formed by the liquid, the substrate, and air leads to outward capillary flows radiating from the center of the drop toward the drying edges.[33]

As the edges of the drop remain pinned to the hydrophilic substrate, a buildup of particles occurs along the substrate edges.[32] At some point during the fabrication, the contact line recedes from the edges. This depinning of the suspension leads to deposition of a thin film of self-assembling material (1−4 μm) as the contact line migrates inward.[34−36]

The particular conditions at which the contact line depins are known to involve multiple experimental parameters.[31,37−40] Critically, the interplay between the solution evaporation rate and the particle diffusion rate is known to affect the depinning of the contact line, and thus the extent of the coffee-ring effect. Minimization of the coffee-ring effect from the drying
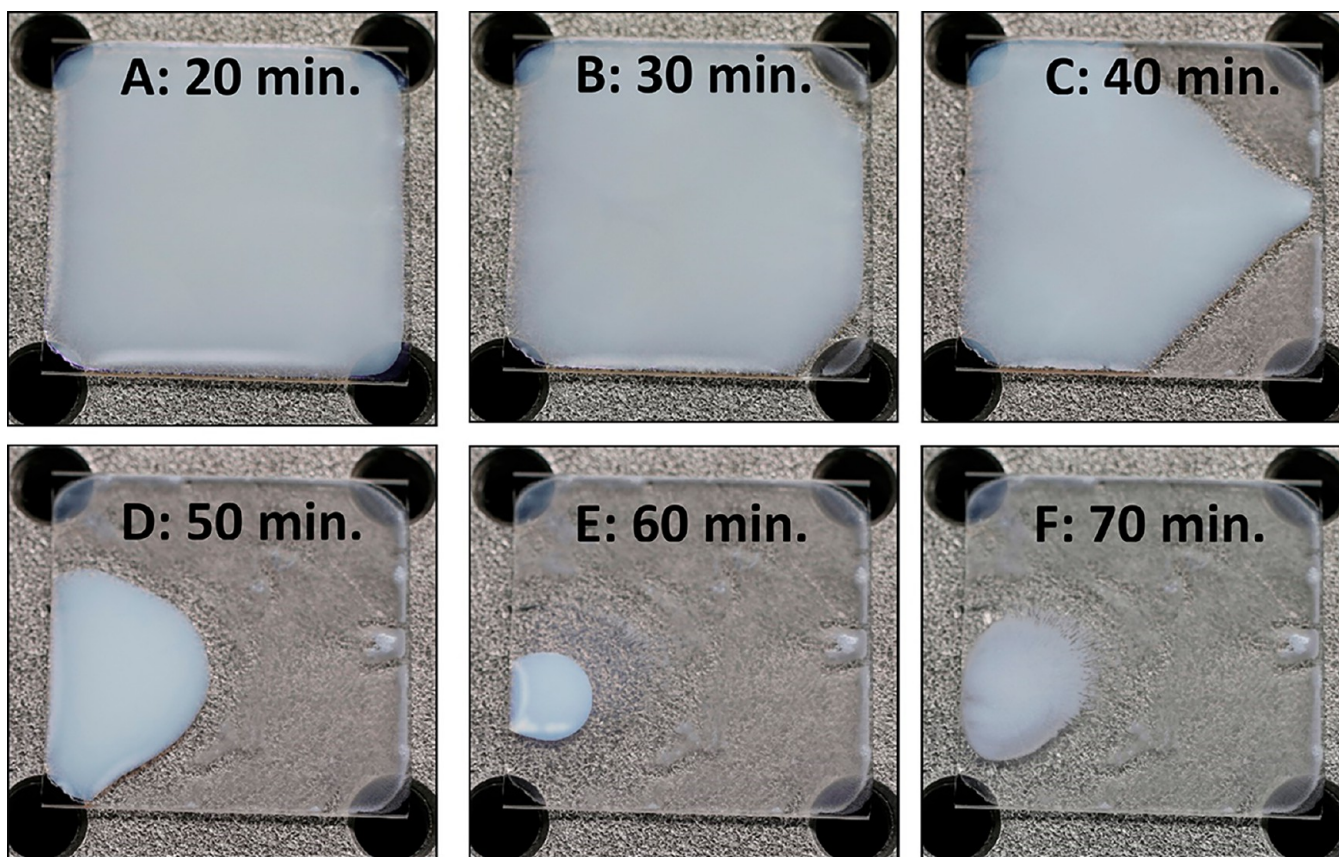
Figure 2. Photographs of a self-assembling PS/SiO$_2$ PhC film taken sequentially following the deposition of 200 μL of PhC precursor solution onto a hydrophilic, fused silica substrate (A−F). The PS/SiO$_2$ PhC film fabrication was carried out at 50% RH and 20 °C using a precursor solution containing ∼4.5 v/v% of hydrolyzed TEOS solution and ∼2.3 v/v% of PSNPs in deionized water. (A) The white appearance of the drying droplet is due to significant light scattering from the colloidal dispersion of PSNPs. (B) After 30 min., the contact line begins to migrate inward from the edges, as evident in the right corners of the substrate. (C−E) The contact line continues to migrate inward, leaving behind a thin film of material, until only a small amount of liquid remains. (F) The self-assembly is complete after ∼80 min. after evaporation of all visible liquid.

suspensions is desired because it yields high quality films of relatively constant thickness.[38,40] These relevant parameters are expected to be sensitive to the particle size, concentration, and the fabrication conditions (i.e., temperature and humidity).

We developed conditions for fabricating PS PhCs based on the work of Yan et al.[21] Using inward-growing self-assembly under ambient laboratory conditions (20 °C and a 50% RH), we fabricated ∼3 μm thick PS PhC films using aqueous dispersions of 2.3 v/v% PSNPs. Time-lapse photographs of the fabrication process indicate that self-assembly is fully complete after 2 h for these samples (Figure S2). Notably, the contact line was observed to depin ∼30 min after the initial deposition of precursor solution, as evident by the inward movement of the drying front.

These results are consistent with the previous report of Yan et. al; however, under our experimental conditions we observe larger stopband extinctions (>1.5 OD) with diffraction bandwidths of ∼20 nm (Figure S3). We conclude that we can also utilize smaller diameter (∼143 nm) PSNPs to fabricate highly ordered PS PhCs.

PS/SiO$_2$ PhC Fabrication Parameters. The addition of hydrolyzed silicates introduces an additional coassembly process during the inward-growing self-assembly of the PhC films.[37,41] The coassembly involves the sol−gel condensation of hydrolyzed silicates into an interconnected SiO$_2$ network (Figure 1). Thus, the first steps in our approach required

optimization of the condensation conditions to generate well-ordered PhCs.[42]

pH Dependence. The first step in the self-assembly involves the fabrication of PS/SiO$_2$ PhCs from a mainly aqueous precursor solution containing monodisperse PSNPs and hydrolyzed TEOS monomers (Figure 1). The presence of HCl, used to catalyze hydrolysis of TEOS, leads to a drop in pH and an increased ionic strength.

Critically, the pH of the PhC precursor solution determines the overall hydrolysis and condensation kinetics of the sol−gel process. Thus, the pH strongly impacts the final SiO$_2$ network morphology.[43] We found that preparing our precursor solutions with an initial pH of 2.7,[42] was optimal for generating contiguous SiO$_2$ networks in our PhCs. Attempts using more neutral pH conditions resulted in poor SiO$_2$ film morphologies (Figure S4).

The presence of HCl (∼0.1 M) also modulates the fused silica substrate surface charges as well as the charge of the PSNPs.[44] Notably, PS PhCs fabricated with HCl, in the absence of TEOS, show film regions that strongly diffract suggesting good ordering (Figure S5). This strong diffraction indicates that the HCl (∼0.1 M) does not inhibit the PSNPs self-assembly into highly ordered arrays.

Evaporation Conditions. The film morphology of PS/SiO$_2$ PhCs fabricated using our modified inward-growing self-assembly also exhibits a distinct "coffee-ring" along the
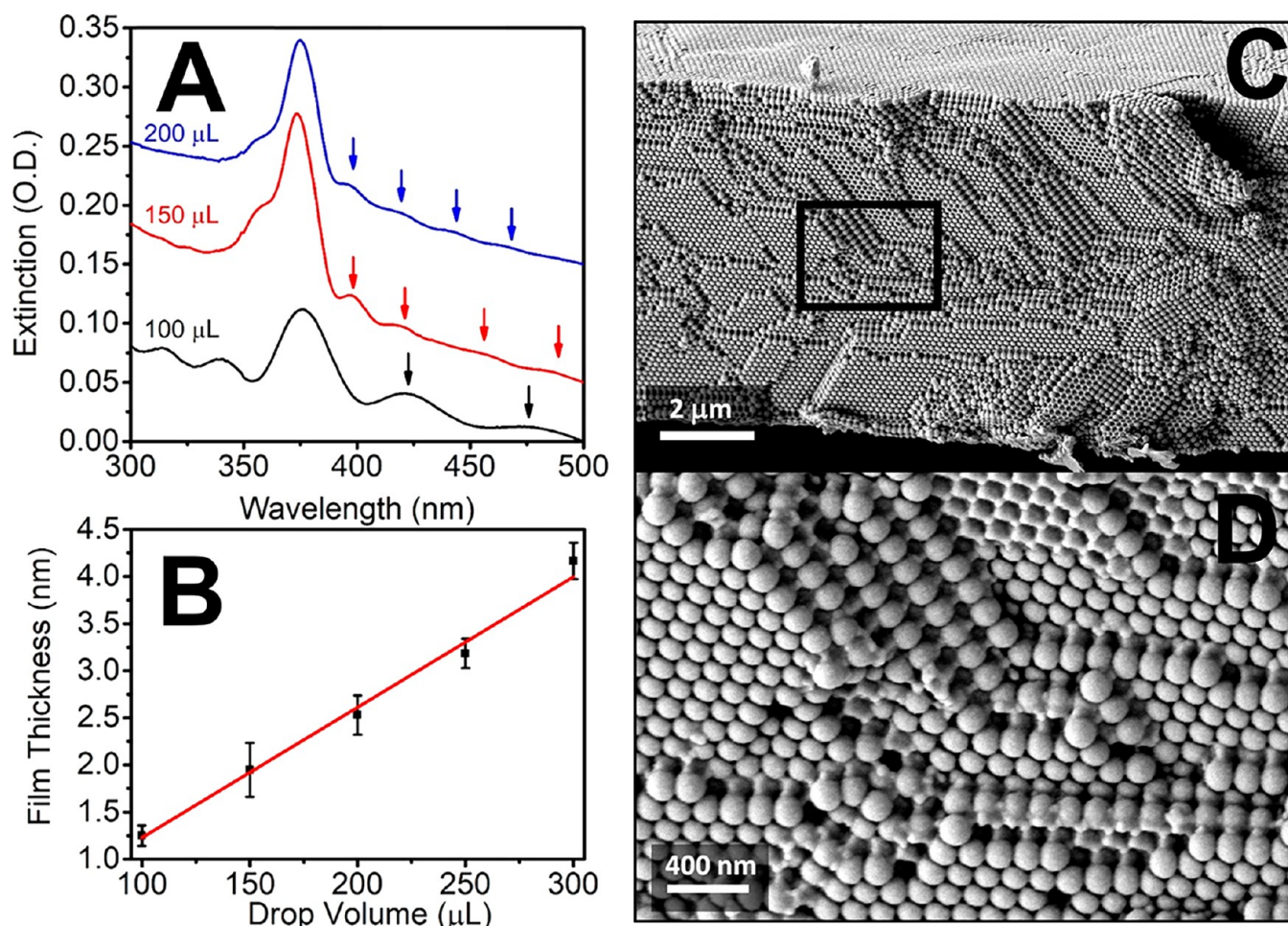
Figure 3. (A) Extinction spectra of PS/SiO$_2$ PhCs fabricated with different volumes of precursor solution. Spectra were vertically offset from each other to facilitate comparison. (B) Dependence of PS/SiO$_2$ PhC film thickness on the volume of the deposited precursor solution. Film thickness was estimated from the spacing of the Fabry–Perot fringes observed in the extinction spectrum (see arrows in panel A) using the relation of Jiang et al.[37] A direct correlation between the film thickness and the drop volume is evident between 100 and 300 μL. The extinction spectra were measured using a rectangular probe beam of ~10 mm height and ~2 mm width. The feature at ~374 nm derives from the stop band of the PS/SiO$_2$ PhC. The precursor solutions contained ~6.0 v/v% of hydrolyzed TEOS solution and 2.3 v/v% of PSNPs in deionized water. (C) Side profile SEM micrograph of a representative regions of a PS/SiO$_2$ PhC. This sample was fabricated using 200 μL of precursor solution. In the presence of hydrolyzed silicates, the space between the PSNPs becomes infilled with a cross-linked, solid, SiO$_2$ network. (D) Higher magnification SEM micrograph collected from the region outlined by a box in C. The close-packing of PSNPs and the formation of a SiO$_2$ network within the voids between them is visible in the micrographs.

substrate edges. These PhCs show relatively homogeneous films over >1 cm^2 areas of the substrate surface. The remaining substrate surface contains a distinct opaque region with a smaller circular void.[21] The formation of these structures can be understood from observations of the film deposition during liquid evaporation during self-assembly.

We carried out the fabrication of a PS/SiO$_2$ PhC under benchtop conditions (20 °C and 50% RH) while photographing the process. Time-lapse photographs of the PS/SiO$_2$ PhC self-assembly show the initial pinning of the contact line (Figure 2A). After ~30 min, the contact line depins and moves inward, depositing a thin film as evident in the right-hand corners of Figure 2B. The location at which the liquid evaporates last corresponds to the highly opaque, circular void region.[21]

Our initial fabrications used partially controlled benchtop conditions (20 °C and 50% RH). However, these resulted in film fabrications that were more susceptible to environmental changes. To allow for more precise control of the solvent

evaporation rate, we carried out subsequent fabrications inside of an environmental control chamber (ECC), which maintains a constant temperature and humidity during self-assembly. The use of an ECC greatly improves the self-assembly reproducibility. For the results presented herein, environment conditions were set to 20 °C and 75% RH, which lead to fabrication times of ~20 h.

The airflows generated inside the ECC perturb the self-assembly process. To obtain reproducible film depositions, we found it critical to minimize the exposure of our samples to these airflows by placing the sample fabrication area under an air shield (vide supra). Low airflow conditions (<20 feet-per-minute, fpm) achieved with the use of an air shield resulted in the formation of visually homogeneous films. These conditions resulted in PS/SiO$_2$ PhCs with better and more consistent optical properties than those fabricated under ambient benchtop conditions.

Optimization of TEOS Volume Percent. Condensation of the hydrolyzed silicate monomers results in the formation of an

interconnected SiO_2 network. Subsequent removal of the PSNPs results in formation of a SiO_2IO (Figure 1C). Insufficient amounts of silicates would result in incomplete filling of the interstices between the PSNPs, which would yield heterogeneous IO structures. High TEOS concentrations could prevent the close-packing of PSNPs into ordered arrays. These concentrations could also generate an SiO_2 overlayer.

We optimized the SiO_2 condensation by varying the v/v% of TEOS solution between 4.5 to >10% in the PhC precursor solution. As the amount of TEOS increased, we observed that the resulting PS/SiO_2 PhC becomes visibly more homogeneous and transparent, up to a value of 8 v/v%.

Addition of greater amounts of TEOS solution resulted in a distinct change in the sample morphology, resulting in highly opaque films with significant delamination defects. On the basis of these observations, we determined the optimal value of TEOS solution to be between ∼6−7 v/v% for suspensions of 2.3 v/v% of PSNPs. We confirmed these results using UV/Vis spectroscopy. We found 6−7 v/v% of TEOS solution produced PhCs with the most reproducible stop band intensities and wavelengths (vide infra).

Structural and Optical Analysis of PS/SiO_2 PhCs. The extinction spectra of PS/SiO_2 films reveal a photonic stopband at ∼370 nm (Figure 3A). SEM micrographs of these materials show close-packed PSNPs arrays infilled by an interconnected SiO_2 network (Figure 3C), with structures consistent with an fcc crystalline arrangement.[45] Thus, it appears that the condensation of SiO_2 only minimally perturbs the formation of the expected close-packed PSNP arrays when using evaporative self-assembly. The observed light diffraction follows Bragg's law (eq 1):

$$m\lambda = 2n_{eff}d \cos \theta \tag{1}$$

In this relation, the wavelength of light (λ) for a particular order (m) diffracted from a crystal with a periodic variation in the index of refraction, is related to the effective refractive index of the material (n_{eff}), the periodicity (d), and the angle (θ) between the reciprocal lattice vector $\bar{G}$ and the incident light wavevector. In our PS/SiO_2 PhCs, the refractive index periodicity arises from the ordered arrangement of the PSNPs and the SiO_2 periodicity.

We note that SEM micrographs of the PhC shows a layer of hexagonally packed spheres on the top surface of the film (Figure 3). Additional layers stacked below define one of the crystallographic (111) axes oriented normal to the film surface (Figure 3, C). Thus, the reciprocal lattice vector $\bar{G}$ for the (111) direction is oriented along the substrate normal. Each of these layers defines a lattice plane, and the distance between them defines the periodicity along the (111) direction (d_{111}). In a totally close-packed structure, a 143 ± 4 nm diameter particle yields a value of 116 ± 3 nm for d_{111}. This value is in excellent agreement with the value of d_{111} estimated from our SEM micrographs, as well as d_{111} of PS PhCs fabricated in the absence of SiO_2 (∼113 nm).

Multiple facets of a PhC domain are visible in the SEM micrographs, revealing additional hexagonally close-packed layers with crystallographic axes oriented about ∼70.5° from the substrate normal (Figure 3, D). We believe these structures suggest that a fcc crystal is present throughout the observed film. We do not observe evidence for hexagonal-close-packed (hcp) or body-centered-cubic (bcc) structures, nor twining, in our SEM micrographs.[45]

Using published values for the index of refraction of PS and SiO_2 of 1.64 and 1.47,[46] and a filling fraction of 0.74 and 0.26, respectively, yields an estimate of n_{eff} of 1.60 for our PS/SiO_2 PhC films. With this value of n_{eff} and a value of d_{111} of 116 nm, we estimate a first order Bragg diffraction of ∼373 nm for light at normal incidence to the film surface. This value qualitatively agrees with the wavelength observed for the stop band maximum as shown in Figure 3A.[47,48] Note that small differences (∼1%) in our estimate for the index of refraction, or of the value of d_{111}, would give rise to changes in the diffracted wavelength of ±4 nm.

PS/SiO_2 Film Thickness. The number of layers in the PhC film determines the overall stop band properties. Increasing the number of layers that participate in diffraction generally increases the diffraction efficiency and decreases the stop band width.[49−51]

Using our optimized compositions for the precursor solutions, PhC films with varying number of layers can be generated by changing the volume of the drop placed on the fused silica substrates. The thickness of these films, and thus the number of layers, can be estimated from the Fabry−Perot interference fringes in the extinction spectra (Figure 3A). These Fabry−Perot fringes arise from interferences between light reflected by the top and bottom surfaces of the PhC film. These fringes indicate a relatively constant film thickness is present in the region sampled by the probing beam.

Following the approach described by Jiang et al.,[37] a linear relation is obtained between the initial droplet volume and the resulting thickness of the PhC films (Figure 3B). Droplet volumes <100 μL did not reliably result in depositions of ordered PhC films. When depositing 100 μL or less of the precursor solution, we observed that the substrate did not completely wet. For droplet volumes higher than 300 μL, the solution tends to leak from the substrate edge, leading to uncontrolled volume loss.

Within this 100−300 μL volume range, we fabricated PS/SiO_2 PhC films with thicknesses varying between 1.25 and 4 μm. Using a conservative estimate for d_{111} of 116 nm, these thicknesses corresponds to between 11 and 35 layers, respectively. Thus, we observe a limit to the thickness of the films that can be fabricated in a single step using inward-growing self-assembly. We are currently exploring other avenues to increase the thickness of these films, either by increasing the v/v% of PSNPs or by adding additional precursor solution during fabrication.

Film Morphology. The drying of colloidal films is well-known to result in cracking defects when these films reach a critical thickness.[31,34−36,52] For an aqueous nanoparticle suspension, the formation of cracks is thought to arise from capillary-induced stresses generated in the film as the solvent evaporates.[39,53] The sample capillary stresses scale with the liquid−air surface tension and inversely with the particle radius.[52,53] Critically, film adhesion to the substrate prevents relaxation of these tensile stresses by constraining further film consolidation once a critical amount of liquid has evaporated.[28,54,55]

The addition of polymers and sol−gel precursors during self-assembly was previously observed to minimize cracking.[20,27] This is thought to allow for the release of drying-generated stresses throughout the polymer network, while likely also minimizing the capillary stresses generated.[28,56−58] On the basis of these results, we examined the morphology of our PS/SiO_2 films using optical profilometry to determine the extent of

crack formation using our modified inward-growing self-assembly approach.

We observe cracking even in ~1 μm thick PS/SiO$_2$ films (Figure 4). We distinctly observe the formation of a ~15 μm
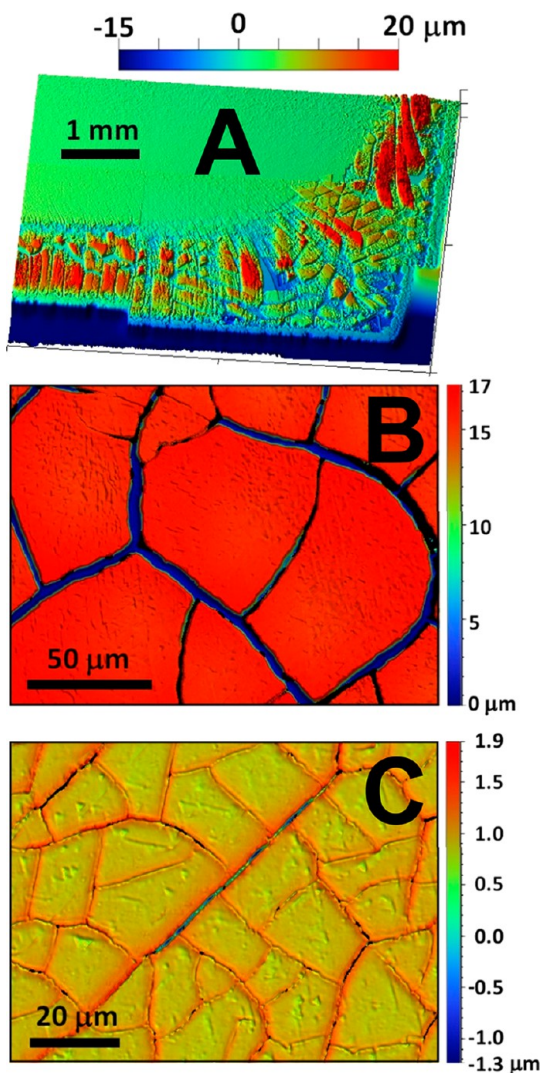

Figure 4. Height maps of a PS/SiO$_2$ PhC film measured using an optical profilometer. The color bars depict the relative height of the observed features. The 3D height map in A was collected at low magnification and it showcases the characteristic "coffee-ring" deposit found at the substrate edge. The height map in B was collected ~0.5 mm from the edge of the substrate, on the "coffee-ring" deposit. The thickness of this "coffee-ring" deposit can be estimated as ~15 μm using the depth of the cracks. The height map in C was collected ~3 mm from the edge of the substrate where the film is ~1 μm thick. Individuals PhC film domains are visible as red and yellow heights relative to the crack-exposed substrate (blue). In addition to film cracking, vacancy defects are evident on the surface of the film. This sample was fabricated using 125 μLs of precursor solution containing ~6.5 v/v% of hydrolyzed TEOS solution and 2.3 v/v% of PSNPs suspended in deionized water.

thick deposit of material at the substrate edge (Figure 4, B). This so-called "coffee ring" has a width of ~1−2 mm. The thickest region of the coffee ring shows relatively low-crack density (~50 μm between cracks), with crack widths of ~5 μm. At regions away from the coffee ring (>3 mm away from the edge), the film thickness does not vary significantly (Figure

4, C). The observed domain sizes are ~15−20 μm in length with <1 μm crack widths. Notably, the surface variability is <300 nm, arising from vacancy defects, as well as partial delamination of the domains due to cracking.[59] In contrast to previous reports for coassembled silicate sol−gel films, we do not observe the triangle-type cracking along (110) planes.[20,27] This observation suggests that with these fabrication conditions, the sol−gel condensation is not extensive enough to avoid film cracking.[60] Notably, the presence of cracking defects does not appear to severely degrade the optical performance of the IO films (vide infra).

Structural and Diffraction Analysis of SiO$_2$ IOs. SiO$_2$ IOs are generated from our PS/SiO$_2$ PhCs by removing the PSNPs template. We found that immersion in piranha solution is very effective in removing PSNPs. Note that to further consolidate the SiO$_2$ network, the PS/SiO$_2$ films are first heated at 70 °C for 2 days prior to removal of the PSNPs. Only treatment with piranha solution produced highly transparent IO films (Figure S6C). In contrast, we observed that calcination at 500 °C to remove the PSNPs results in extensive film shrinkage as reported previously.[61] Immersion of our PS/SiO$_2$ films in THF does not completely remove the PSNPs. This results in visually evident incoherent light scattering (Figure S6B).

SEM Analysis of IOs. Figure 5 shows SEM micrographs of a SiO$_2$ IO generated using our fabrication protocol. The surface of this IO shows the periodic arrangement of air spheres in a SiO$_2$ network. Isolated sphere vacancies and nanocracks are visible on the top (111) layer. These are generally located near the center of the individual IO film domains (Figure 5A). The side profile SEM micrograph of the IO is consistent with a close-packed fcc arrangement of air spheres (Figure 5B).[45]

The presence of three subfeatures for each void is clearly discernible at higher magnifications and reveals the 3-point sphere-to-sphere contacts between the top layer and the one below (Figure 5C). Clear observation of these features indicates good ordering between the top two IO layers.[37,41] The surface roughness of the SiO$_2$ network observed at the ~10−20 nm scale derives from the condensation of hydrolyzed silicates. For instance, SiO$_2$ films fabricated in the absence of PSNPs display similar surface morphologies (Figure S7).

Deep UV Light Extinction of IOs. On the basis of the periodic nanoscale structure observed in the SEM micrographs of our SiO$_2$ IOs, these PhCs should diffract deep UV light. Indeed, the transmittance of an IO measured at normal incidence ($\theta = 0°$ in eq 1) shows an optical stop band centered at ~227 nm (Figure 6A). At this wavelength, the maximum light attenuation is ~68%. In wavelength regions away from the stop band maximum, light attenuation is ~37% at 200 nm and <25% at >400 nm. These findings suggest that a fraction of the light attenuated at the stop band wavelengths derives from incoherent scattering. Using the background attenuation, we can quantify the incoherent light scattering losses at the stop band as ~35%. Furthermore, by measuring the stop band attenuation relative to the background we estimate a diffraction efficiency of ~32%.

We propose that the ratio of these values can be used as a metric to quantify the performance of PhCs using only the transmission spectra. The ratio of the peak diffraction efficiency to the incoherent scattering loss considers contributions from both of these light attenuation processes to the photonic stop band maximum.
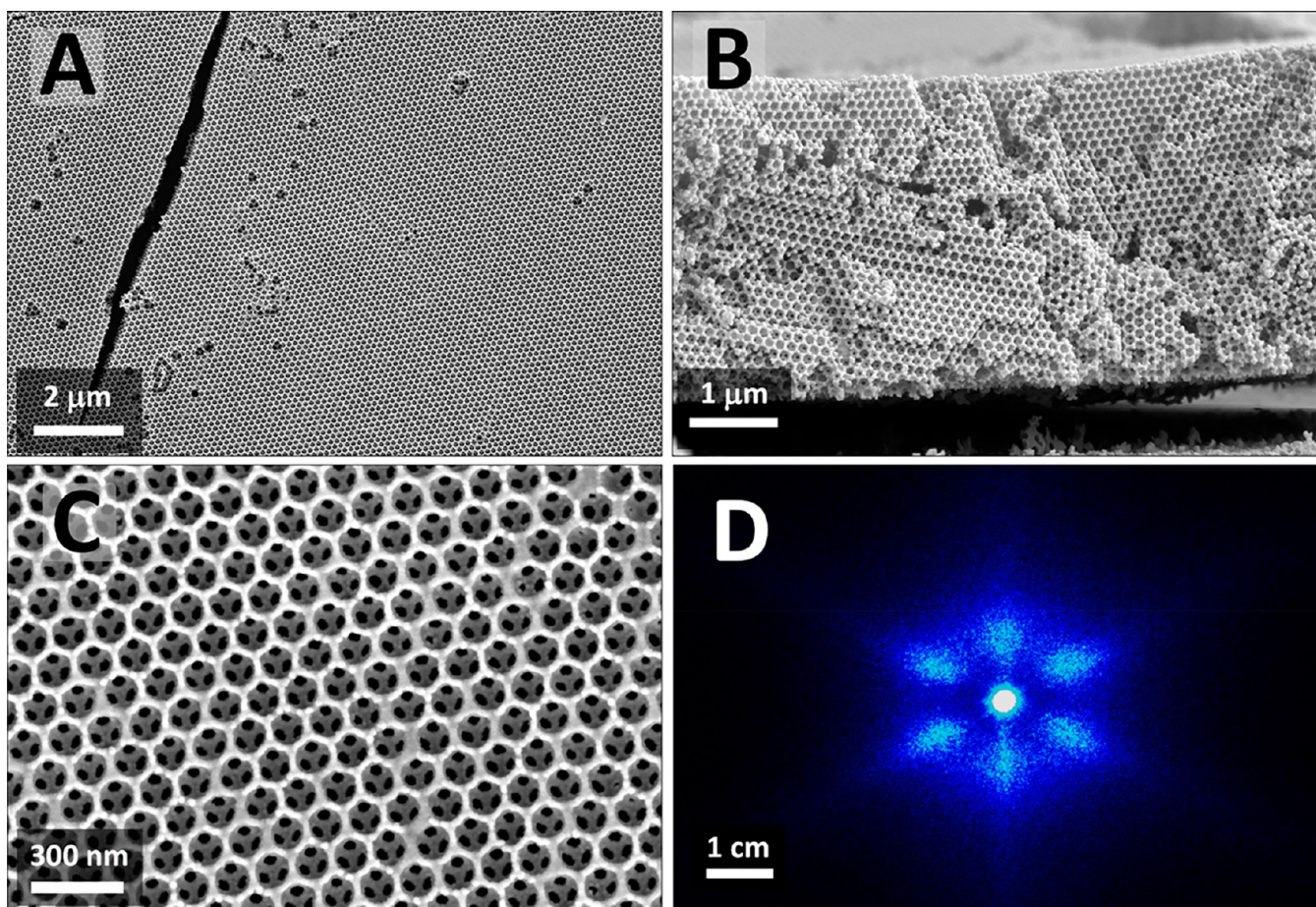
Figure 5. SEM micrographs from representative regions of a SiO$_2$ IO. (A) Viewing along the substrate normal, the putative fcc (111) surface can be discerned. Isolated defects in the form of nanocracks and sphere vacancies are also evident. (B) Side-view SEM micrograph from a SiO$_2$ IO show a structure consistent with the presence of an fcc arrangement of air spheres surrounded by a SiO$_2$ network. (C) At higher magnifications of the fcc (111) surface, the periodic ordering of spherical air voids and condensed SiO$_2$ can be clearly observed. Note the presence of 3 interior dark spots at each air sphere, indicating contact points between the air spheres. The prevalence of this motif across the observed domains indicates excellent ordering between the top (111) layer and the one below. (D) Diffraction of a 213 nm laser beam from the surface of a SiO$_2$IO, imaged on fluorescent paper ~0.25 m away from the IO surface. A central bright spot is observed, surrounded by 6 less intense lobes. The symmetry of the diffraction pattern is derived from the hexagonal symmetry of the top surface of the IO, indicating that the crystal orientation observed in Figure 5B is largely maintained across the ~1 mm^2 area probed.

It is essential to note that, for the IO sample shown in Figure 6, this ratio is ~0.9. This performance ratio is the highest yet reported for IOs diffracting in the deep UV (<400 nm). Our previously fabricated SiO$_2$ IOs using vertical self-assembly showed a ratio of <0.2. Increasing the diffraction efficiency, or decreasing the incoherent scattering losses, would increase the performance ratio further. Notably, CCAs used for our previous state-of-the-art UV hyperspectral Raman imaging instrument had a performance ratio >4.[3]

We attribute the incoherent scattering losses to light scattering from nonperiodic modulations of the PhC refractive index. Presumably, these losses arise from a variety of defects. However, based on our results, we hypothesize that these losses are minimized as the ordering of the PSNPs increases. In general, we observe that increased incoherent scattering correlates with visually evident optically heterogeneous IOs.

Overall, the incoherent scattering losses from our IOs fabricated using inward growing self-assembly is low and is of similar magnitude to that of solid, crack-free PhCs with visible light diffraction.[20,41,57,58]

Angular Dependence of Diffraction and Film Thickness. The wavelengths diffracted by our SiO$_2$IO can be tuned by changing the beam incidence angle relative to the crystal.[29,62] We observe a monotonic blue-shift in the stop band maximum as the beam incident angle increases (Figure 6A). When the incidence angle is increased to 25°, the stop band maximum shifts ~18 nm. This behavior can be accurately modeled by using the Bragg–Snell relation,[18,63,64] using values $n_{eff} = 1.12 \pm 0.01$ and $d_{111} = 102 \pm 1$ nm (Figure 6A, inset).

For comparison, n_{eff} can be estimated for our IO with eq 2, using an index of refraction of SiO$_2$ at 227 nm of 1.53[46] and an air sphere filling fraction φ of 0.74[64−66]

$$n_{eff}(\lambda) = n_{air} \times \varphi_{air} + n_{SiO_2}(1 - \varphi_{air}) \tag{2}$$

The estimated value of 1.14 for n_{eff} is in good agreement with the value obtained using the Bragg–Snell fit. In contrast, the value for d_{111} is much smaller than expected. Notably, estimates of d_{111} obtained from side-profile SEM micrographs from analogous IOs exhibit similar shrinkages.

Previous reports of SiO$_2$ IOs have also reported a shrinkage of the SiO$_2$ matrix along the substrate normal due to silanol
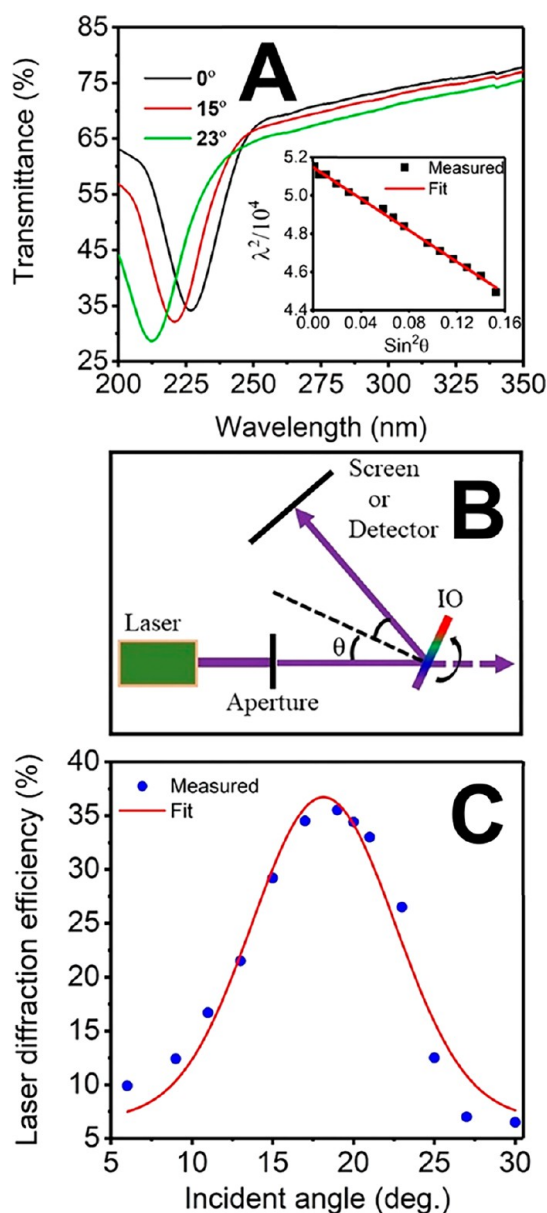
Figure 6. (A) Transmission spectra of a SiO_2 IO sample obtained at various incident angles. The incident angle is defined as the angle formed between beam propagation direction and the surface normal. The putative fcc IO (111) direction is along the film surface normal. A linear fit of λ^2 versus $\sin^2(\theta)$, shown in the inset, was used to determine that n_{eff} and d_{111} are 1.12 ± 0.01 and 102 ± 1 nm, respectively. (B) Experimental setup used to measure the power of a 213 nm laser beam diffracted by the IO shown in A. The IO was fixed on a rotational mount and the laser incidence angle (θ) was varied in increments of 2 degrees. An aperture was used to limit the beam diameter to ~1 mm. (C) Diffraction efficiency as a function of angle (blue dots). The diffracted beam power was measured using a power meter ~10 cm from the IO surface. This power was ratioed to the apertured laser source power (~10 mW). At the Bragg angle, the measured diffraction efficiency is ~30%. A Gaussian fit to the experimental data (red curve) was used to estimate the diffraction angular bandwidth. We observe the fwhm, $\Delta\theta$, as $9° \pm 1°$ (equiv. to $\Delta\lambda = 12 \pm 1$ nm).

condensation.[20,29,61,62] We posit that this shrinkage can be partially mitigated by chemically capping the unreacted silanol groups during removal of the PSNPs.

The thickness of our IO can be estimated by measuring the reflection spectrum using a collimated, white-light LDLS (Figure S8). The most intense peak observed at ~220 nm is due to diffraction of the LDLS beam. Fabry–Perot fringes arising from the interference of light beams reflected by the top and bottom surfaces of the IO film are evident at higher wavelengths. Fabry–Perot fringes have been observed previously for PhCs fabricated from silica nanospheres.[37] These Fabry–Perot fringes indicate that the film thickness is relatively constant over regions probed by the ~2 mm diameter probe beam. Thus, the spacing between the λ_{max} of the fringes can be used to estimate the thickness of the IO film.[20,37,67]

Using the relations described by Jiang et al. and the value of 1.14 for n_{eff} yields a film thickness of 2.10 ± 0.02 μm. This thickness is consistent with that of PS/SiO_2 PhCs fabricated using analogous preparations, as estimated using Fabry–Perot oscillations (vide supra). Using the value of d_{111} estimated from our Bragg–Snell fit, this thickness corresponds to ~21 layers.

Far Field Diffraction Image of SiO_2 IOs. The far field image of a 213 nm laser beam diffracted from our IO was visualized using a fluorescent screen (Figures 5D and 6B). The observed diffraction pattern shows a bright central spot surrounded by six less intense lobes arranged in a hexagonal pattern. The presence of these well-oriented, discrete lobes indicates that the PhC array orientation is relatively constant over the IO region probed by our ~1 mm^2 diameter laser beam.

The hexagonal symmetric diffraction pattern from our IO is reminiscent of the 2D diffraction patterns previously reported for CCAs. This pattern was attributed to diffraction from the outer (111) layer in well-ordered CCAs.[23] Discrete spots arranged in a hexagonally symmetric pattern have also been observed for close-packed FCC PS PhCs,[68] 2D optical gratings,[69] and 2D photonic crystals with a hexagonal lattice.[18,70]

Thus, we posit that the hexagonal symmetry of the 213 nm laser diffraction from our IO arises from the 2D hexagonal symmetry of the outer (111) planes. While the bright central spot largely follows Bragg's Law of diffraction (vide supra), we posit that the surrounding 6 lobes derive from the hexagonal symmetry of the IO PhC surface, which constitutes the basis for the 2D diffraction (Figure 5C).

IO PhC 213 nm Diffraction. To better quantify the diffraction bandwidths ($\Delta\lambda$) and efficiencies (η), we measured the diffraction of highly collimated 213 nm laser light from our SiO_2 IO.[3,20] We measured the power diffracted at the bright central spot (Figure 5D) as a function of incidence angle and used a Gaussian fit to model the angular diffraction band shape (Figure 6C).

Maximum diffraction is observed when $\theta = 19°$. The diffraction shows an angular full-width at half-max (fwhm) of $9° \pm 1°$. We measure a peak Bragg diffraction efficiency of ~30% using ~10 mW of 213 nm laser light incident onto the IO. This value is in good agreement with the diffraction efficiency estimated using the transmittance spectrum (Figure 6, A). This is a 5-fold improvement in performance over that of our previously fabricated SiO_2 IOs.[20] To estimate $\Delta\lambda$ from our power vs incident angle intensities, we used the Bragg–Snell relation to convert the angular fwhm to $\Delta\lambda$. This procedure yields a bandwidth of 12 ± 1 nm (Figure 6C). This value of $\Delta\lambda$ is ~28% smaller than those observed for SiO_2 IO fabricated by other approaches.[20] We attribute these improvements in

efficiency and bandwidth to a decrease in defects and an increased ordering of the SiO_2 network.[30]

We note that our $\Delta\lambda$ obtained from laser diffraction measurements is generally smaller than the $\Delta\lambda$ determined by extinction spectra (Figure S9). This behavior arises from a lack of collimation of the spectrometer beam used to measure the extinction.

While the diffraction bandwidths of our IOs are broader than those observed for CCAs,[3,23,51] this increase breadth may not be unexpected when considering the large refractive index contrast (Ψ) of these SiO_2 IO films. For comparison, highly ordered poly-allyl methacrylate (PAMA, n = 1.64) IOs with 295 nm air−sphere diameters exhibit normalized diffraction bandwidths $\Delta\lambda/\lambda$ of ∼0.07 (with Ψ = −0.465).[49] This value is analogous to the $\Delta\lambda/\lambda$ value of our SiO_2 IO film of ∼0.06 (for Ψ = −0.427).

Due to the large value of our IO refractive index contrast, light meeting the Bragg condition is strongly attenuated by the (111) layers of the SiO_2 IO. This limits the number of layers that can effectively participate in diffraction. For comparison, a much greater number of layers are sampled in diffraction by low Ψ PhCs such as CCAs (Ψ ∼ 0.01). This low Ψ diffraction gives rise to much narrower values of $\Delta\lambda$. These observations suggest that further decreases in $\Delta\lambda$ of our IOs can be achieved by decreasing Ψ.

The scalar wave approximation (SWA) provides an appropriate framework by which to analyze the optical properties of high dielectric contrast PhCs.[49] A defined parameter is the critical number of layers, N_c, required to attenuate 50% of the incident light meeting the Bragg condition at normal incidence.[50,51] For our IO, N_c is ∼7 layers.[49] Given the large number of layers present in our SiO_2 IOs (∼20), we expect that our IOs films should exhibit higher diffraction efficiencies than we observe.

IO Performance and Technological Applications. For optical applications, the principal metrics to evaluate IO performance are the scattering losses, the diffraction efficiency (η), and the diffraction bandwidth ($\Delta\lambda$). Considering the low incoherent scattering losses observed in our IOs, we believe that the presence of cracks and delamination defects are the primary factors currently limiting their performance for general applications.

The presence of cracks in the IO contribute to the refractive index inhomogeneity that allows some part of the incident light to transmit, reducing the measured value of η. Thus, we expect that the diffraction efficiency from of IOs can be further improved by minimizing the crack defect density, possibly by using lower surface tension dispersants during self-assembly and minimizing substrate−film interactions.[31,58]

On the basis of our observations, fabricating thinner films of <1 μm is expected to yield improvements in η, as film cracking is minimized under these conditions. Alternatively, preparation of alumina IOs using a comparable sol−gel coassembly approach might also yield improved diffraction efficiencies due to the increased refractive index of alumina over silica in the deep UV (∼1.9 vs ∼1.5 at 213 nm, respectively).[46] However, these alumina IOs are expected to have increased values for $\Delta\lambda$.

For hyperspectral imaging applications, the implementation of these IO materials is limited by the relatively large value of $\Delta\lambda$ (∼12 nm). For example, our previous hyperspectral Raman imaging devices were implemented using a photonic crystal with ∼60% diffraction efficiency as a WSD.[3] With improved

spectrometer design, it is feasible to develop a device using a photonic crystal with ∼30% diffraction efficiency. However, Raman imaging applications require a diffraction bandwidth $\Delta\lambda$ on the order of ∼1 nm due to the narrow wavelength range of typical UV Raman spectra.

Fabrication of such ultranarrow $\Delta\lambda$ IOs represents a challenging task, as these materials require highly ordered PhCs of significant thickness. For example, the air voids of our IOs can be infiltrated with appropriate materials that can decrease the refractive index contrast (Ψ) of the photonic crystal. It is well-known that this reduces the fwhm of the photonic stop band. However, because of the decrease in Ψ, this approach also dramatically decreases the diffraction efficiency (Figure S10). Thus, to fabricate IOs with $\Delta\lambda$ < 1 nm, additional layers in the form of thicker films are required. On the basis of these findings, we posit that fabrication of 10-fold thicker, highly ordered IOs represents the next step in developing these materials for Raman imaging applications.

■ CONCLUSION

We fabricated and characterized nanoporous SiO_2 IO films that diffract 213 nm laser light with ∼30% efficiency. To generate these materials, we prepared close-packed fcc PS/SiO_2 PhCs by using a coassembly approach whereby monodisperse PSNPs and hydrolyzed silicates are deposited onto a hydrophilic fused silica substrate. Upon controlled evaporation of the liquid, the PSNPs self-assemble into close-packed arrays due to capillary forces.

Concurrently, a SiO_2 network is formed within the interstices of the spheres via the condensation of hydrolyzed silicates. Removal of the PSNPs yields an SiO_2IO film of ∼2 μm thickness with ∼70% light attenuation at the Bragg condition.

Detailed studies of the IO diffraction using 213 nm laser light indicates ∼30% of the incident light is diffracted at the expected Bragg angle into a narrow beam with <1° divergence. From these results, we estimate the magnitude of the incoherent scattering losses to be ∼35%. The experimentally measured diffraction bandwidth of 12.3 nm is in good agreement with the value expected from the large refractive index contrast of the IO. These findings indicate that our adaptation of inward growing self-assembly yields IOs with improved diffraction efficiencies and reduced incoherent scattering losses relative to previously published approaches. Notably, our IOs show the best optical performance of any previously fabricated deep UV PhC.

We are currently exploring further optimizations to our fabrication conditions, with the goal of reducing film cracking, while increasing film thickness, and further minimizing surface defects. We expect that additional improvements in the film morphology will further minimize incoherent scattering which will greatly enhance the diffraction efficiency of these materials.

■ ASSOCIATED CONTENT

ⓢ Supporting Information

The Supporting Information is available free of charge at https://pubs.acs.org/doi/10.1021/acsanm.0c00309.

> Details about the synthesis of monodisperse PSNPs, spectroscopic characterization of PS PhCs, and time-lapse photographs of self-assembly of PhCs, as well as additional details regarding the optimization of PhC fabrication parameters (PDF)

■ AUTHOR INFORMATION

Corresponding Authors

Ivan G. Pallares − *Department of Chemistry, University of Pittsburgh, Pittsburgh, Pennsylvania 15260, United States;* ● orcid.org/0000-0001-5209-983X; Email: ivp3@pitt.edu

Sanford A. Asher − *Department of Chemistry, University of Pittsburgh, Pittsburgh, Pennsylvania 15260, United States;* ● orcid.org/0000-0003-1061-8747; Email: asher@pitt.edu

Authors

Dipak Rout − *Department of Chemistry, University of Pittsburgh, Pittsburgh, Pennsylvania 15260, United States*

Thomas J. Deering − *Department of Chemistry, University of Pittsburgh, Pittsburgh, Pennsylvania 15260, United States;* ● orcid.org/0000-0001-8406-2230

Kyle T. Hufziger − *Department of Chemistry, University of Pittsburgh, Pittsburgh, Pennsylvania 15260, United States;* ● orcid.org/0000-0001-6057-8232

Sergei V. Bykov − *Department of Chemistry, University of Pittsburgh, Pittsburgh, Pennsylvania 15260, United States;* ● orcid.org/0000-0002-6161-0027

Complete contact information is available at:
https://pubs.acs.org/10.1021/acsanm.0c00309

Author Contributions

[†]I.G.P. and D.R. contributed equally to this work. D.R. started the experimental effort to fabricate SiO₂ Inverse Opals by horizontal self-assembly. I.G.P. and D.R. and T.J.D. planned and executed experiments. I.G.P., D.R., and T.J.D. contributed to the writing of the manuscript. K.T.H provided the nanoparticles. S.V.B provided expertise on equipment. S.A.A. supervised the research program. All authors have given approval and contributed to the final version of the manuscript.

Notes

The authors declare no competing financial interest.

■ REFERENCES

(1) Hufziger, K. T.; Bykov, S. V.; Asher, S. A. Raman Hyperspectral Imaging Spectrometer Utilizing Crystalline Colloidal Array Photonic Crystal Diffraction. *Appl. Spectrosc.* **2014**, *68* (11), 1219−1223.

(2) Gares, K. L.; Hufziger, K. T.; Bykov, S. V.; Asher, S. A. Review of Explosive Detection Methodologies and the Emergence of Standoff Deep UV Resonance Raman. *J. Raman Spectrosc.* **2016**, *47* (1), 124−141.

(3) Hufziger, K. T.; Bykov, S. V.; Asher, S. A. Ultraviolet Raman Wide-Field Hyperspectral Imaging Spectrometer for Standoff Trace Explosive Detection. *Appl. Spectrosc.* **2017**, *71* (2), 173−185.

(4) *The Raman Effect: A Unified Treatment of the Theory of Raman Scattering by Molecules*; Long, D. A., Ed.; John Wiley & Sons, Ltd.: New York, NY, 2002.

(5) Asher, S. A.; Flaugh, P.; Washinger, G. Crystalline Colloidal Bragg Diffraction Devices: The Basis for a New Generation of Raman Instrumentation. *Spectroscopy* **1986**, *1* (12), 26−31.

(6) Flaugh, P. L.; O'Donnell, S. E.; Asher, S. A. Development of a New Optical Wavelength Rejection Filter: Demonstration of its Utility in Raman Spectroscopy. *Appl. Spectrosc.* **1984**, *38* (6), 847−850.

(7) Wang, L.; Tikhonov, A.; Asher, S. A. Silica Crystalline Colloidal Array Deep Ultraviolet Narrow-Band Diffraction Devices. *Appl. Spectrosc.* **2012**, *66* (4), 426−431.

(8) Yablonovitch, E. Inhibited Spontaneous Emission in Solid-State Physics and Electronics. *Phys. Rev. Lett.* **1987**, *58* (20), 2059.

(9) John, S. Strong Localization of Photons in Certain Disordered Dielectric Superlattices. *Phys. Rev. Lett.* **1987**, *58* (23), 2486.

(10) Bermel, P.; Luo, C.; Zeng, L.; Kimerling, L. C.; Joannopoulos, J. D. Improving Thin-Film Crystalline Silicon Solar Cell Efficiencies with Photonic Crystals. *Opt. Express* **2007**, *15* (25), 16986−17000.

(11) Guldin, S.; Huttner, S.; Kolle, M.; Welland, M. E.; Muller-Buschbaum, P.; Friend, R. H.; Steiner, U.; Tetreault, N. Dye-Sensitized Solar Cell Based on a Three-Dimensional Photonic Crystal. *Nano Lett.* **2010**, *10* (7), 2303−2309.

(12) Lončar, M.; Yoshie, T.; Scherer, A.; Gogna, P.; Qiu, Y. Low-Threshold Photonic Crystal Laser. *Appl. Phys. Lett.* **2002**, *81* (15), 2680−2682.

(13) Cao, W.; Munoz, A.; Palffy-Muhoray, P.; Taheri, B. Lasing in a Three-Dimensional Photonic Crystal of the Liquid Crystal Blue Phase II. *Nat. Mater.* **2002**, *1* (2), 111.

(14) Ellis, B.; Mayer, M. A.; Shambat, G.; Sarmiento, T.; Harris, J.; Haller, E. E.; Vučković, J. Ultralow-Threshold Electrically Pumped Quantum-Dot Photonic-Crystal Nanocavity Laser. *Nat. Photonics* **2011**, *5* (5), 297.

(15) Lee, K.; Asher, S. A. Photonic Crystal Chemical Sensors: pH and Ionic Strength. *J. Am. Chem. Soc.* **2000**, *122* (39), 9534−9537.

(16) Asher, S. A.; Alexeev, V. L.; Goponenko, A. V.; Sharma, A. C.; Lednev, I. K.; Wilcox, C. S.; Finegold, D. N. Photonic Crystal Carbohydrate Sensors: Low Ionic Strength Sugar Sensing. *J. Am. Chem. Soc.* **2003**, *125* (11), 3322−3329.

(17) Rout, D.; Vijaya, R. Localized Surface Plasmon-Influenced Fluorescence Decay in Dye-Doped Metallo-Dielectric Opals. *J. Appl. Phys.* **2016**, *119* (2), 023108.

(18) Armstrong, E.; O'Dwyer, C. Artificial Opal Photonic Crystals and Inverse Opal Structures − Fundamentals and Applications from Optics to Energy Storage. *J. Mater. Chem. C* **2015**, *3* (24), 6109−6143.

(19) Péré, E.; Cardy, H.; Cairon, O.; Simon, M.; Lacombe, S. Quantitative Assessment of Organic Compounds Adsorbed on Silica Gel by FTIR and UV−VIS Spectroscopies: The Contribution of Diffuse Reflectance Spectroscopy. *Vib. Spectrosc.* **2001**, *25* (2), 163−175.

(20) Hufziger, K. T.; Zrimsek, A. B.; Asher, S. A. Solid Deep Ultraviolet Diffracting Inverse Opal Photonic Crystals. *ACS Applied Nano Materials* **2018**, *1* (12), 7016−7024.

(21) Yan, Q.; Zhou, Z.; Zhao, X. S. Inward-Growing Self-Assembly of Colloidal Crystal Films on Horizontal Substrates. *Langmuir* **2005**, *21* (7), 3158−3164.

(22) Nair, R. V.; Vijaya, R. Structural and Optical Characterization of Photonic Crystals Synthesized Using the Inward Growing Self-Assembling Method. *Appl. Phys. A: Mater. Sci. Process.* **2008**, *90* (3), 559−563.

(23) Asher, S. A.; Weissman, J. M.; Tikhonov, A.; Coalson, R. D.; Kesavamoorthy, R. Diffraction in Crystalline Colloidal-Array Photonic Crystals. *Phys. Rev. E* **2004**, *69* (6), 066619.

(24) Reese, C. E.; Guerrero, C. D.; Weissman, J. M.; Lee, K.; Asher, S. A. Synthesis of Highly Charged, Monodisperse Polystyrene Colloidal Particles for the Fabrication of Photonic Crystals. *J. Colloid Interface Sci.* **2000**, *232* (1), 76−80.

(25) Abràmoff, M. D.; Magalhães, P. J.; Ram, S. J. Image Processing with ImageJ. *Biophotonics International* **2004**, *11* (7), 36−42.

(26) Bykov, S. V.; Mao, M.; Gares, K. L.; Ashera, S. A. Compact Solid-State 213 nm Laser Enables Standoff Deep Ultraviolet Raman Spectrometer: Measurements of Nitrate Photochemistry. *Appl. Spectrosc.* **2015**, *69* (8), 895−901.

(27) Hatton, B.; Mishchenko, L.; Davis, S.; Sandhage, K. H.; Aizenberg, J. Assembly of Large-Area, Highly Ordered, Crack-Free

Inverse Opal Films. *Proc. Natl. Acad. Sci. U. S. A.* **2010**, *107* (23), 10354−10359.

(28) Zhou, J.; Wang, J.; Huang, Y.; Liu, G.; Wang, L.; Chen, S.; Li, X.; Wang, D.; Song, Y.; Jiang, L. Large-Area Crack-Free Single-Crystal Photonic Crystals via Combined Effects of Polymerization-Assisted Assembly and Flexible Substrate. *NPG Asia Mater.* **2012**, *4*, No. e21.

(29) Waterhouse, G. I. N.; Waterland, M. R. Opal and Inverse Opal Photonic Crystals: Fabrication and Characterization. *Polyhedron* **2007**, *26* (2), 356−368.

(30) Kaplan, C. N.; Wu, N.; Mandre, S.; Aizenberg, J.; Mahadevan, L. Dynamics of Evaporative Colloidal Patterning. *Phys. Fluids* **2015**, *27* (9), 092105.

(31) Routh, A. F. Drying of Thin Colloidal Films. *Rep. Prog. Phys.* **2013**, *76* (4), 046603.

(32) Deegan, R. D.; Bakajin, O.; Dupont, T. F.; Huber, G.; Nagel, S. R.; Witten, T. A. Capillary Flow as the Cause of Ring Stains from Dried Liquid Drops. *Nature* **1997**, *389* (6653), 827−829.

(33) Popov, Y. O. Evaporative Deposition Patterns: Spatial Dimensions of the Deposit. *Phys. Rev. E* **2005**, *71* (3), 036313.

(34) Holmes, D. M.; Tegeler, F.; Clegg, W. J. Stresses and Strains in Colloidal Films During Lateral Drying. *J. Eur. Ceram. Soc.* **2008**, *28* (7), 1381−1387.

(35) Chiu, R. C.; Garino, T. J.; Cima, M. J. Drying of Granular Ceramic Films: I, Effect of Processing Variables on Cracking Behavior. *J. Am. Ceram. Soc.* **1993**, *76* (9), 2257−2264.

(36) Chiu, R. C.; Cima, M. J. Drying of Granular Ceramic Films: II, Drying Stress and Saturation Uniformity. *J. Am. Ceram. Soc.* **1993**, *76* (11), 2769−2777.

(37) Jiang, P.; Bertone, J. F.; Hwang, K. S.; Colvin, V. L. Single-Crystal Colloidal Multilayers of Controlled Thickness. *Chem. Mater.* **1999**, *11* (8), 2132−2140.

(38) Shen, X.; Ho, C.-M.; Wong, T.-S. Minimal Size of Coffee Ring Structure. *J. Phys. Chem. B* **2010**, *114* (16), 5269−5274.

(39) Goehring, L.; Clegg, W. J.; Routh, A. F. Solidification and Ordering during Directional Drying of a Colloidal Dispersion. *Langmuir* **2010**, *26* (12), 9269−9275.

(40) Li, Y.; Yang, Q.; Li, M.; Song, Y. Rate-Dependent Interface Capture Beyond the Coffee-Ring Effect. *Sci. Rep.* **2016**, *6*, 24628.

(41) Wong, S.; Kitaev, V.; Ozin, G. A. Colloidal Crystal Films: Advances in Universality and Perfection. *J. Am. Chem. Soc.* **2003**, *125* (50), 15589−15598.

(42) Belton, D. J.; Deschaume, O.; Perry, C. C. An Overview of the Fundamentals of the Chemistry of Silica with Relevance to Biosilicification and Technological Advances. *FEBS J.* **2012**, *279* (10), 1710−1720.

(43) *Sol−Gel Science: The Physics and Chemistry of Sol-Gel Processing*; Brinker, C. J., Scherer, G. W., Eds.; Academic Press, Inc.: San Diego, CA, 1990.

(44) Sulpizi, M.; Gaigeot, M.-P.; Sprik, M. The Silica−Water Interface: How the Silanols Determine the Surface Acidity and Modulate the Water Properties. *J. Chem. Theory Comput.* **2012**, *8* (3), 1037−1047.

(45) Guo, W.; Wang, M.; Xia, W.; Dai, L. Evaporation-Induced Self-Assembly of Capillary Colloidal Crystal in a Face-Centered Cubic Structure with Controllable Thickness. *J. Mater. Res.* **2012**, *27* (13), 1663−1671.

(46) Rodríguez de Marcos, L. V.; Larruquert, J. I.; Méndez, J. A.; Aznárez, J. A. Self-Consistent Optical Constants of SiO_2 and Ta_2O_5 films. *Opt. Mater. Express* **2016**, *6* (11), 3622−3637.

(47) Partridge, R. H. Vacuum-Ultraviolet Absorption Spectrum of Polystyrene. *J. Chem. Phys.* **1967**, *47* (10), 4223−4227.

(48) Story, V. M.; McIntyre, D.; O'Mara, J. H. Solvent Effects on the Ultraviolet Absorption of Polystyrene. *J. Res. Natl. Bur. Stand., Sect. A* **1967**, *71A* (2), 169−175.

(49) Bertone, J. F.; Jiang, P.; Hwang, K. S.; Mittleman, D. M.; Colvin, V. L. Thickness Dependence of the Optical Properties of Ordered Silica-Air and Air-Polymer Photonic Crystals. *Phys. Rev. Lett.* **1999**, *83* (2), 300−303.

(50) Spry, R. J.; Kosan, D. J. Theoretical Analysis of the Crystalline Colloidal Array Filter. *Appl. Spectrosc.* **1986**, *40* (6), 782−784.

(51) Rundquist, P. A.; Photinos, P.; Jagannathan, S.; Asher, S. A. Dynamical Bragg Diffraction from Crystalline Colloidal Arrays. *J. Chem. Phys.* **1989**, *91* (8), 4932−4941.

(52) Singh, K. B.; Tirumkudulu, M. S. Cracking in Drying Colloidal Films. *Phys. Rev. Lett.* **2007**, *98* (21), 218302.

(53) van der Kooij, H. M.; van de Kerkhof, G. T.; Sprakel, J. A Mechanistic View of Drying Suspension Droplets. *Soft Matter* **2016**, *12* (11), 2858−2867.

(54) Huang, Y.; Zhou, J.; Su, B.; Shi, L.; Wang, J.; Chen, S.; Wang, L.; Zi, J.; Song, Y.; Jiang, L. Colloidal Photonic Crystals with Narrow Stopbands Assembled from Low-Adhesive Superhydrophobic Substrates. *J. Am. Chem. Soc.* **2012**, *134* (41), 17053−17058.

(55) Xia, T.; Luo, W.; Hu, F.; Qiu, W.; Zhang, Z.; Lin, Y.; Liu, X. Y. Fabrication of Crack-Free Photonic Crystal Films on Superhydrophobic Nanopin Surface. *ACS Appl. Mater. Interfaces* **2017**, *9* (26), 22037−22041.

(56) Zhu, Z.; Zhang, J.; Wang, C.-F.; Chen, S. Construction of Hydrogen-Bond-Assisted Crack-Free Photonic Crystal Films and Their Performance on Fluorescence Enhancement Effect. *Macromol. Mater. Eng.* **2017**, *302* (6), 1700013.

(57) Yi, B.; Shen, H. Facile Fabrication of Crack-Free Photonic Crystals with Enhanced Color Contrast and Low Angle Dependence. *J. Mater. Chem. C* **2017**, *5* (32), 8194−8200.

(58) Kanai, T.; Sawada, T. New Route to Produce Dry Colloidal Crystals without Cracks. *Langmuir* **2009**, *25* (23), 13315−13317.

(59) Zhang, J.; Lu, Y.; He, L.; Yang, L.; Ni, Y. Modeling Progressive Interfacial Debonding of a Mud-Crack Film on Elastic Substrates. *Eng. Fract. Mech.* **2017**, *177*, 123−132.

(60) Rao, S.; Shaw, R.; Rout, D.; Kumar, G.; Vijaya, R.; Gupta, S. Diffraction Imaging of Cracks in Self-Assembled Photonic Crystals. *Opt. Mater.* **2019**, *91*, 189−194.

(61) Phillips, K. R.; Vogel, N.; Hu, Y.; Kolle, M.; Perry, C. C.; Aizenberg, J. Tunable Anisotropy in Inverse Opals and Emerging Optical Properties. *Chem. Mater.* **2014**, *26* (4), 1622−1628.

(62) Schroden, R. C.; Al-Daous, M.; Blanford, C. F.; Stein, A. Optical Properties of Inverse Opal Photonic Crystals. *Chem. Mater.* **2002**, *14* (8), 3305−3315.

(63) Aguirre, C. I.; Reguera, E.; Stein, A. Tunable Colors in Opals and Inverse Opal Photonic Crystals. *Adv. Funct. Mater.* **2010**, *20* (16), 2565−2578.

(64) Lonergan, A.; McNulty, D.; O'Dwyer, C. Tetrahedral Framework of Inverse Opal Photonic Crystals Defines the Optical Response and Photonic Band Gap. *J. Appl. Phys.* **2018**, *124* (9), 095106.

(65) Nishijima, Y.; Ueno, K.; Juodkazis, S.; Mizeikis, V.; Misawa, H.; Tanimura, T.; Maeda, K. Inverse Silica Opal Photonic Crystals for Optical Sensing Applications. *Opt. Express* **2007**, *15* (20), 12979−12988.

(66) Using a simple average instead of the Dudre model results in a 2.1% decrease in the estimated value for a filling fraction of 0.74.

(67) *Optics*, 4th ed.; Hetch, E., Ed.; Pearson Education, Limited: England, 2016.

(68) Kedia, S.; Kumar, A.; Singh, R. P. Investigation of Local Structural Properties of Self-Assembled Photonic Crystals by Optical Diffraction. *Appl. Phys. B: Lasers Opt.* **2012**, *108* (4), 903−907.

(69) Piccolo, V.; Chiappini, A.; Armellini, C.; Barozzi, M.; Lukowiak, A.; Sazio, P.-J.; Vaccari, A.; Ferrari, M.; Zonta, D. 2D Optical Gratings Based on Hexagonal Voids on Transparent Elastomeric Substrate. *Micromachines* **2018**, *9* (7), 345.

(70) Smith, N. L.; Coukouma, A.; Dubnik, S.; Asher, S. A. Debye Ring Diffraction Elucidation of 2D Photonic Crystal Self-Assembly and Ordering at the Air−Water Interface. *Phys. Chem. Chem. Phys.* **2017**, *19* (47), 31813−31822.